

Microwave-Assisted Synthesis of Fe₃O₄ Nanocrystals with Predominantly Exposed Facets and Their Heterogeneous UVA/Fenton Catalytic Activity

Yuanhong Zhong,[†] Lin Yu,^{*,†} Zhi-Feng Chen,[‡] Hongping He,[§] Fei Ye,[†] Gao Cheng,[†] and Qianxin Zhang[‡]

[†]School of Chemical Engineering and Light Industry, Guangdong University of Technology, Guangzhou 510006, China

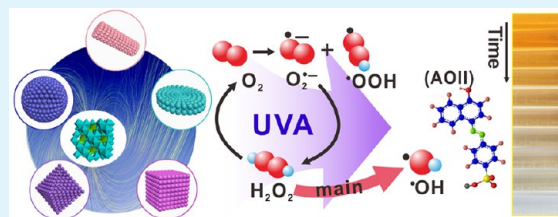
[‡]Institute of Environmental Health and Pollution Control, School of Environmental Science and Engineering, Guangdong University of Technology, Guangzhou 510006, China

[§]CAS Key Laboratory of Mineralogy and Metallogeny, Guangzhou Institute of Geochemistry, Chinese Academy of Sciences, Guangzhou 510640, China

Supporting Information

ABSTRACT: Fe₃O₄ nanocrystals with five different morphologies (i.e., nanospheres, nanorods, nanocubes, nano-octahedrons, and nanoplates) were acquired using a simple, efficient, and economic microwave-assisted oxidation technique. The microstructure, morphology, predominant exposed facets, and iron atom local environment of Fe₃O₄ were revealed by powder X-ray diffraction (PXRD), scanning transmission electron microscopy (SEM), high-resolution transmission electron microscopy (HRTEM), X-ray photoelectron spectrometer (XPS), and Mössbauer spectrum. We demonstrated that the heterogeneous UVA/Fenton catalytic activities of Fe₃O₄ nanocrystals are morphology/facets dependent. Under UVA irradiation, the catalytic activity of the as-prepared Fe₃O₄ was in the sequence of nanospheres > nanoplates > nano-octahedrons ≈ nanocubes > nanorods > nano-octahedrons (by coprecipitation). The dominating factor for the catalytic performance was the particle size and BET specific surface area; moreover, the exposed {111} facets, which contained more Fe²⁺ species, on the nanocrystal surface led to a stronger UVA/Fenton catalytic activity. Both •OH and O₂•⁻ radicals participated in the UVA/Fenton degradation process, and •OH played the dominant role. These morphology-controlled nanomagnetites showed great potential in applications as heterogeneous UVA/Fenton catalysts for effectively treating nonbiodegradable organic pollutants.

KEYWORDS: Fe₃O₄, exposed facets, microwave synthesis, nanocrystals, UVA/Fenton



1. INTRODUCTION

As a ubiquitous mineral on the earth's surface (e.g., sediments, aerosol, and various weathered products), magnetite (Fe₃O₄) is a promising natural mineral. Due to the high surface redox activity, strong electron transport capability, and environmental compatibility, the application of magnetite as catalysts in heterogeneous Fenton technology has received widespread attention. To the best of our knowledge, previous studies have largely focused on the physicochemical properties, the magnetite-based advanced materials, and some applications in different industrial fields.^{1,2} However, little attention has been paid to the effect of micromorphology and structure interface on the heterogeneous Fenton catalytic activity of magnetite for the degradation of organic pollutants.³ The crystalline phase, sizes, and anisotropic morphologies of nanomaterial greatly influence their physicochemical properties and surface reactivity.⁴ For instance, Hu et al.⁵ indicated the Co₃O₄ nanobelts with predominantly exposed {011} planes were more active for the reduction of CO than Co₃O₄ nanocubes with exposed {001} planes. The hematite (α-Fe₂O₃) nanorods show higher

catalytic activity than the nanotubes and nanocubes for methane combustion and CO oxidation.⁶ With the exposure of more reactive (100) and (110) facets, the CeO₂ nanorods were more active for CO oxidation than the spherical, cubic, or octahedral nanoparticles.⁴ Zhang's group⁷ revealed that both Bi₂₅FeO₄₀ microcubes and microsphere with exposed facets of {001} exhibited high photo-Fenton catalytic activity, whereas Bi₂₅FeO₄₀ tetrahedral with exposed facets of {111} showed low catalytic activity. Specific to the use of Fe₃O₄ as Fenton catalysts, significant progress has been made with respect to substituted cations,^{8–10} supported materials,¹¹ species, and properties of organic pollutants (e.g., methylene blue, phenol and acid orange II, Tetrabromobisphenol A).^{12–14} However, previously reported Fe₃O₄ particles tend to be octahedral or spherical in shape, and the size and morphology of particles are seldom discussed. Recently, Hou et al.³ demonstrated that the

Received: May 16, 2017

Accepted: July 31, 2017

Published: July 31, 2017

activity of nanorods nanoparticles (NPs) was greater than that of the microcubes or microspheres; however, the authors did not take into account the nanosize effect and exposed reactive crystal planes of the particles. It is also unknown whether the magnetite NPs, with different exposed crystal facets and micromorphologies, affect the catalysis of organic degradation, which is of great importance for understanding the reactivity of magnetite NPs.

Unlike other iron (hydr)oxides, Fe_3O_4 uniquely contains both Fe^{2+} and Fe^{3+} in an inverse spinel structure, which is written as $[\text{Fe}^{3+}]_{\text{tet}}[\text{Fe}^{2+}\text{Fe}^{3+}]_{\text{oct}}\text{O}_4$. With the ordering of a face-centered-cubic (FCC) structure, magnetite is endowed with a general sequence of surface energies, $\gamma\{111\} < \gamma\{100\} < \gamma\{110\} < \gamma\{220\}$,¹⁵ meaning the magnetite crystals are surrounded mostly by $\{111\}$ lattice planes and generally exhibit octahedral morphology. In other words, the growth rate of $\{111\}$ planes is quicker than that of other planes, and the octahedral shapes are the thermodynamically favored morphology according to the Wulff construction. In recent years, rapid developments in the field of nanoscience have enabled the fabrication of novel morphological and structural nanomaterials. With the advantages of simplicity, ease of control, and low cost, liquid-phase methods became the essential and powerful approaches toward preparing nanomaterials with controlled morphology. For the past decade, several important liquid-phase methods, including coprecipitation,¹⁶ hydrothermal synthesis,¹⁷ microemulsion,¹⁸ sol–gel synthesis,¹⁹ thermal decomposition,²⁰ and ultrasound-assisted methods,²¹ have been applied to synthesize magnetite with various morphologies. To date, magnetite with spherical, octahedral, cubic, wire, rod, tubular, and flower-like micromorphologies are easily obtained for a few specific applications.²² Nevertheless, these methods separately or simultaneously suffer from the following drawbacks: (i) poor yield; (ii) time-consuming; (iii) requirement of organic solvents, such as phenylether,²³ tetracosane,²⁴ benzyl ether,²⁵ oleylamine,²⁶ mixture of 1,2-hexadecanediol, oleic acid, and oleylamine;²³ and (iv) complicated manipulation or multistep synthesis.²⁷ Therefore, a simple, efficient, and economic method is highly desired.

Generally, microwave chemistry offers great advantages, such as rapid processing, simplicity, and high-energy efficiency, compared to conventional methods.²⁸ Under microwave irradiation, numerous novel structures with various shapes, such as TiO_2 nanowires,²⁹ $\alpha\text{-Fe}_2\text{O}_3$ nanorings,³⁰ 3D flower-like $\alpha\text{-Ni}(\text{OH})_2$,³¹ V_2O_5 nanorods,³² Fe_3O_4 nanowires, and rose-like nanoparticles,³³ have been prepared. To expand upon this idea, we developed a microwave irradiation oxidation route for the preparation of Fe_3O_4 NPs with controlled morphologies. The fine crystal structure characteristics of the Fe_3O_4 NPs were evaluated in detail via various techniques. The morphology- and facet-dependence of the heterogeneous UVA/Fenton catalytic activity of Fe_3O_4 NPs were compared by degradation of the probe molecule acid orange II, and the major active species as well as the reusability were also investigated. The obtained results are of great significance for further understanding the correlation between the catalytic properties and nanocrystal morphology. Additionally, the results provide an important experimental basis for regulating the morphology of nanomagnetite. Furthermore, this work may promote further exploration of potential applications of nanomagnetite with more reactive crystal planes in heterogeneous Fenton catalysis.

2. MATERIALS AND METHODS

2.1. Preparation of Magnetite Nanoparticles. All chemicals and reagents employed in this study were analytical grade and used as received. Magnetite samples with different micromorphologies (i.e., nanospheres, nanorods, nanocubes, nano-octahedrons, and nanoplates) were synthesized by a simple and efficient microwave-assisted oxidation process. Ferrous sulfate heptahydrate and nitrate were used as the only iron source and weak oxidizing agent, respectively. The synthetic procedure is as follows: $\text{FeSO}_4 \cdot 7\text{H}_2\text{O}$ was dissolved in a three-neck round-bottom flask containing 60 mL of deionized water. The same volume of lye containing NaOH , NaNO_3 and a few drops of hydrazine hydrate was added dropwisely to the above solution and stirred continuously. After that, different amounts (Table S1) of polyethylene glycol (PEG-600) or polyvinylpyrrolidone (PVP, $M_w = 58000$) were added to the suspension, followed by ultrasonic dispersion for 10 min. Subsequently, the reflux reaction was heated by microwave oven at 95 °C for 30–60 min with an output power of 600 W. The reaction system was cooled to room temperature, and the black product was separated by a magnet and washed with distilled water and absolute ethanol several times. Finally, the black product was freeze-dried under vacuum at -80 °C for 48 h. The morphology of the synthesized magnetite particles was controlled by adjusting the amounts of glacial acetic acid, sodium hydrate, and PEG/PVP. The detailed reagent additions of each sample are provided in Table S1 in the Supporting Information. The samples were denoted as $\text{Fe}_3\text{O}_4\text{-M}$, -S, -R, -C, -O, and -P, where M represents the surface morphology of the particles, S for nanospheres, R for nanorods, C for nanocubes, O for nano-octahedrons, and P for nanoplates. A magnetite sample synthesized by the normal coprecipitation method ($\text{Fe}_3\text{O}_4\text{-N}$) was used to compare the catalytic activities of the magnetite samples.

2.2. Characterization of Magnetite Samples. PXRD patterns were collected on a Bruker D8 advance diffractometer equipped with a Lynxeyeone-dimensional solid-state detector and $\text{Cu K}\alpha$ radiation (40 kV and 40 mA) at room temperature. The recorded angular range was from 10° to 80° (2θ) with a scanning step width of 0.02° and speed of 4° min^{-1} . BET specific surface area was measured by nitrogen physisorption on a Quantachrome Instruments Quadrasorb SI surface area and pore size analyzer, after degassing at 110 °C for 12 h. XPS was performed on a Thermo ESCALAB 250XI multifunctional imaging electron spectrometer, equipped with monochromatic $\text{Al K}\alpha$ ($h\nu = 1486.6 \text{ eV}$) radiation. Curve fitting was carried out by XPS PEAK4.1 software using a Gaussian–Lorentz peak shape and Shirley background function. The binding energies of Fe 2p and O 1s were determined, and the carbon signal (C 1s) at 284.8 eV was taken as a reference for binding energy calibration. SEM measurements were obtained on a Hitachi 8020 using 2 kV accelerating voltage. HRTEM was taken with a FEI Tecnai G2 F20 S-Twin operating at 200 kV. Nanocrystal morphology, size distributions, and lattice fringes were analyzed with a Gatan software Digital Micrograph (TM) 3.7.4. Room-temperature (297 K) ^{57}Fe Mössbauer spectra were collected using an Austin Science S-600 spectrometer. The γ -ray radioactive source was $^{57}\text{Co}/\text{Rh}$ and placed perpendicularly incident on the magnetite samples. The proportion counter was used for detecting transmitted photons. A standard sample $\alpha\text{-Fe}$ foil was used as reference for calibrating the isomer shift. All the Mössbauer spectra were fitted with the least-squares fitting algorithm using MossWinn 4.0 program. The magnetic parameters were measured by a Quantum Design MPMS XL-7 SQUID magnetometer. Magnetic susceptibility M – H curves were conducted at room temperature, where M is the magnetization and H is the applied magnetic field ($\pm 2\text{T}$).

2.3. Heterogeneous UVA/Fenton Catalytic Activity. The heterogeneous Fenton catalytic activities of six as-prepared magnetite samples were evaluated comparatively by degradation of a probe molecule, acid orange II (AOII), in water under UVA irradiation. The tests were carried out on a photochemical reaction instrument with a hollow cylindrical quartz tube photoreactor (XPA-7, Nanjing XUJ Co. Ltd.). A 5 W UVA lamp ($\lambda = 365 \text{ nm}$) was used as the light source for the irradiation reaction. The detailed experimental procedures for

degradation of AOII are described in detail in the Supporting Information (Text S1).

Hydroxyl radicals ($\cdot\text{OH}$) and superoxide radical ($\text{O}_2^{\cdot-}$) produced during the photocatalytic degradation process were estimated by Electron Spin Resonance (ESR), using dimethylpyridine N-oxide (DMPO) as a capture agent. The ESR spin-trapped signals of the radicals were measured on a Bruker E500 spectrometer with 0.5 g L^{-1} magnetite sample and 50 mmol DMPO under UVA irradiation ($\lambda = 365 \text{ nm}$). The detections of $\cdot\text{OH}$ and $\text{O}_2^{\cdot-}$ were carried out in deionized water (after adjustment to $\text{pH} = 3$) and methanol media, respectively. The ESR was processed with the center field at 323 mT, microwave frequency of 9.057 GHz, power of 0.998 mW, sweep width of 5 mT, sweep time of 1.0 min, and time constant of 0.03 s.

3. RESULTS AND DISCUSSION

3.1. Microstructure and Morphology of Fe_3O_4 . Figure 1 shows the XRD patterns of the Fe_3O_4 samples, and all samples

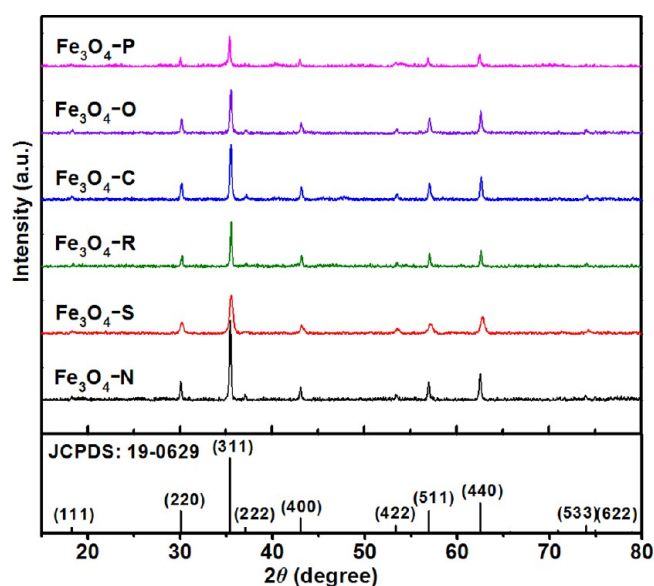


Figure 1. PXRD of the synthetic magnetite samples.

had well-crystallized spinel structures corresponding to the standard card of magnetite (JCPDS: 19-0629). A slight difference in the full width at half-maximum and relative intensities of the diffraction peaks was found at 30.1° , 35.4° , 43.0° , and 62.5° , which are assigned to (311), (220), (400), and (440) planes of Fe_3O_4 , respectively. This implies that there are differences in the crystal sizes and the preferred orientation. Preferred growth orientation in magnetite has been widely reported, and it is known that the surface free energy plays a

pivotal role.^{15,34} Table 1 displays the lattice constant a_0 , BET surface area, and particle size of the Fe_3O_4 NPs. Narrow, sharp peaks for Fe_3O_4 -N were found, and its lattice constant a_0 was similar to the theoretical value (8.396 Å) of magnetite. By comparison, the peaks for the Fe_3O_4 -S and Fe_3O_4 -P samples were slightly broadened with decreased intensities, revealing that the crystallite sizes of these two samples were smaller than that of Fe_3O_4 -N. Accordingly, bigger lattice parameters were observed (Table 1). As for the Fe_3O_4 -R, Fe_3O_4 -C, and Fe_3O_4 -O samples, the smaller lattice parameters were probably attributed to the formation of the bigger nanocrystalline structure (Table 1). It should be noted that the mean crystallite size of samples was calculated using the Debye–Scherrer’s formula; therefore, the lattice distortion was ignored during the calculation. The black color of the samples and lattice parameter suggested that the NPs mainly consist in magnetite. As shown in Table 1, the BET surface areas of the magnetite samples synthesized by microwave-assisted oxidation process were higher than that of the coprecipitation derived Fe_3O_4 -N sample (only $16 \text{ m}^2 \text{ g}^{-1}$). The smaller spherical and nanorod samples possessed significantly higher surface areas, 46 and $43 \text{ m}^2 \text{ g}^{-1}$, respectively.

The size and morphology of Fe_3O_4 NPs were further investigated by SEM (Figure 2) and (HR) TEM (Figure 3). Fe_3O_4 -N grew mainly in an octahedral shape (Figure 2a) with an average size of about 123 nm ($n \approx 50$ particles). Obviously, these octahedral particles were large in size and agglomerate with limited dispersion. The spherical, rod-like, cubic, octahedral, and plate-like morphologies of Fe_3O_4 NPs were confirmed from Figure 2b–f. Figure 2b and the inset (TEM image) exhibit the detailed morphology of Fe_3O_4 -S, revealing a uniform spherical morphology without specific orientation. The average diameter of Fe_3O_4 -S, determined by statistical analysis of the TEM measurements, was 25 nm, which is quite close to the observed crystal sizes from XRD (22.2 nm). This result implies that the Fe_3O_4 -S nanocrystals were highly mono-dispersed in particle-size distribution. Fe_3O_4 -R nanocrystals were 13–35 nm in lateral size and 45–150 nm in longitudinal lengths, while the mean particle sizes of Fe_3O_4 -C and Fe_3O_4 -O were about 40 and 93 nm, respectively. These values were significantly smaller than that of Fe_3O_4 -N. Fe_3O_4 -P given in Figure 2f, which shows the average lateral size and thickness about 87 and 19 nm, respectively.

More detailed microstructural information on the Fe_3O_4 NPs was obtained by TEM and HRTEM. Figure 3 displays the lattice fringes (upper right insets) and the fast Fourier transforms (FFT) of HRTEM images (lower right insets) taken from an individual particle. Fe_3O_4 -N and Fe_3O_4 -O NPs

Table 1. Lattice Parameters, BET Surface Areas, and Particle Sizes of the Magnetite Samples

samples	morphology	$a_0/\text{Å}$	D^a/nm	mean size ^b /nm	size range/nm	SSA ^c /m ² g ⁻¹
Fe_3O_4 -N	nano-octahedrons	8.393	41.3	lateral size, 123	70–180	16
Fe_3O_4 -S	nanosphere	8.405	22.2	diameter, 25	13–41	46
Fe_3O_4 -R	nanorods	8.373	51.0	lateral size, 23 length, 97	13–35 45–150	43
Fe_3O_4 -C	nanocubes	8.380	43.0	side-lengths, 40	29–60	19
Fe_3O_4 -O	nano-octahedrons	8.382	43.6	lateral size, 93	60–136	21
Fe_3O_4 -P	nanoplates	8.403	35.3	lateral size, 87 thickness, 19	57–164 15–28	25

^a D is the mean crystallite size evaluated from the XRD patterns using the Debye–Scherrer’s formula. ^bMean size is the average particle size measured from the SEM/TEM images. ^cSSA is the specific surface area evaluated using the BET model.

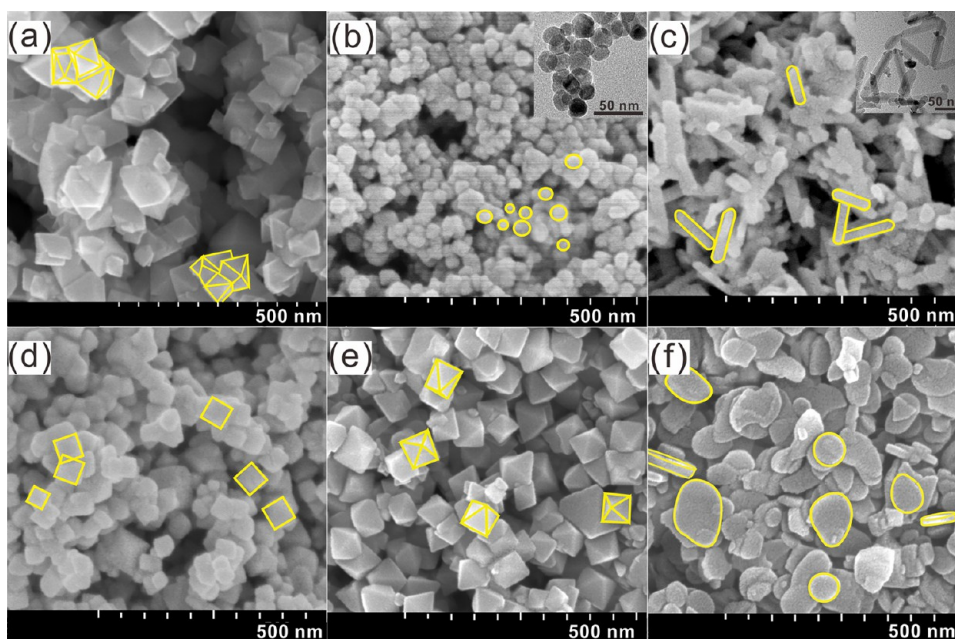


Figure 2. SEM images of the magnetite NPs, (a): $\text{Fe}_3\text{O}_4\text{-N}$, (b): $\text{Fe}_3\text{O}_4\text{-S}$, (c): $\text{Fe}_3\text{O}_4\text{-R}$, (d): $\text{Fe}_3\text{O}_4\text{-C}$, (e): $\text{Fe}_3\text{O}_4\text{-O}$, (f): $\text{Fe}_3\text{O}_4\text{-P}$, inset in (b) and (c): TEM of samples $\text{Fe}_3\text{O}_4\text{-S}$ and $\text{Fe}_3\text{O}_4\text{-R}$.

represented the typical octahedral shape of magnetite (Figure 3a,e), and clear atomic lattice fringes could be observed. The measured lattice spacing (d values) of the crystallographic planes was approximately 0.485 nm, rather close to the $\{111\}$ lattice planes of Fe_3O_4 crystal (JCPDS: 19-0629). Additionally, the FFT patterns shown in the inset corresponded closely to the diffraction from the crystal planes of Fe_3O_4 . This suggests that the $\text{Fe}_3\text{O}_4\text{-N}$ and $\text{Fe}_3\text{O}_4\text{-O}$ NPs were enclosed by $\{111\}$ planes and form octahedral shapes. The $\text{Fe}_3\text{O}_4\text{-S}$ NPs (Figure 3b) were single crystalline with a nearly spherical shape. The d values (0.295 nm) estimated from the HRTEM image and the corresponding FFT patterns (Figure 3b) were assigned to the $\{220\}$ planes of Fe_3O_4 . As dictated by thermodynamics, the quasi-spherical shape was possibly enclosed by a mix of $\{111\}$ and $\{100\}$ facets to minimize the total surface energy.^{35,36} Well-dispersed rod-shape Fe_3O_4 particles can be found in Figure 3c. The observed d values were approximately 0.175 nm, and were similar to that of $\{422\}$ lattice planes of magnetite. Based on the intersection angle between the lattice planes $\{211\}$ and growth direction (30.0°), the $\text{Fe}_3\text{O}_4\text{-R}$ particles seemed to grow along the $[110]$ direction. Several particles were analyzed simultaneously (Figure S1), and this analysis confirmed that the $\text{Fe}_3\text{O}_4\text{-R}$ particles grew preferentially to the $[110]$ direction and were likely capped by $\{311\}$ facets and sidewalls of the nanorods, mainly exposing the $\{112\}$ and $\{110\}$ facets. Figure 3d presents particles with perfect cubic shapes, with lattice spacing measured at 0.297 and 0.301 nm. These values were similar to the standard d spacing of $\{220\}$ at 0.297 nm for magnetite. In addition, the lattice planes deduced from the indexed FFT spot patterns were $\{400\}$ planes with interplanar spacing of 2.10 nm. This phenomenon infers that the electron beam was incident along the $[001]$ crystallographic orientation of Fe_3O_4 , and the spot array was in agreement with the extinction rule of electron diffraction of SG $Fd\bar{3}m$.³⁷ This means Fe_3O_4 nanocubes had cubic symmetry and $\{100\}$ faceted planes.³⁸ For the $\text{Fe}_3\text{O}_4\text{-P}$ NPs, the FFT pattern (lower right inset of Figure 3f) showed an obvious splitting phenomenon, suggesting that nanoplates have a twin-crystal structure.

Furthermore, lattice spacing of 0.254 and 0.840 nm for nanoplate particles matched well with the (311) and (100) lattice planes of magnetite. Additionally, the involved lattice planes deduced from the thickness direction (i.e., the longitudinal direction) were (400) and (111) planes with interplanar spacing of 0.210 and 0.485 nm. It has been reported that in the case of $\text{FeO}/\text{Fe}_3\text{O}_4$ NPs such a structure would form due to twinned nuclei along the $[111]$ direction.³⁹ More specifically, such a thin plate-like structure covered by the $\{111\}$ facets at the top and bottom surfaces ($>70\%$ of the surface), and side faces ($<30\%$ of the surface) was bound by $\{100\}$ and $\{111\}$ facets, as well as stacking faults and/or twin defects along the vertical direction.⁴⁰

The surface element composition and element valence state were investigated using XPS based on the specific binding energy. The Fe 2p XPS spectra (Figure 4a) of the Fe_3O_4 NPs show the characteristic doublet located at 709.7–710.6 eV and 723.3–723.9 eV, which corresponded to Fe 2p_{3/2} and Fe 2p_{1/2}, respectively. It is suggested that Fe^{III} (Fe_2O_3) and Fe^{II} (FeO) states coexist in magnetite structures.⁴¹ Taking $\text{Fe}_3\text{O}_4\text{-R}$ for example (Figure 4b), the measured Fe 2p_{3/2} (Fe 2p_{1/2}) binding energies were 709.4 eV (722.8 eV) for Fe^{II} and 710.9 eV (724.4 eV) for Fe^{III}. These results are in good agreement with previously reported spectra of Fe_3O_4 .⁴² Similarly, the XPS spectra of the other samples were also fitted by corresponding function and parameters (Figure S2), and their fitted parameters are tabulated in Table S2. There was a small satellite peak around 718 eV (peak 5), which was likely attributed to the air-oxidized surface of Fe_3O_4 to $\gamma\text{-Fe}_2\text{O}_3$ during sample storage and the XPS preparation procedure. The O 1s photoelectron spectra of all Fe_3O_4 samples are displayed in Figure S3. The recorded O 1s spectra were resolved into two main peaks at about 529.9 and 531.2 eV, which were ascribed to the lattice oxygen (Fe–O) and adsorbed oxygen or surface hydroxyl species (–OH), respectively.^{43,44} An additional peak at higher binding energy around 532.5 eV was assigned to surface-adsorbed water found in $\text{Fe}_3\text{O}_4\text{-N}$, $\text{Fe}_3\text{O}_4\text{-S}$, and $\text{Fe}_3\text{O}_4\text{-P}$.⁴⁵

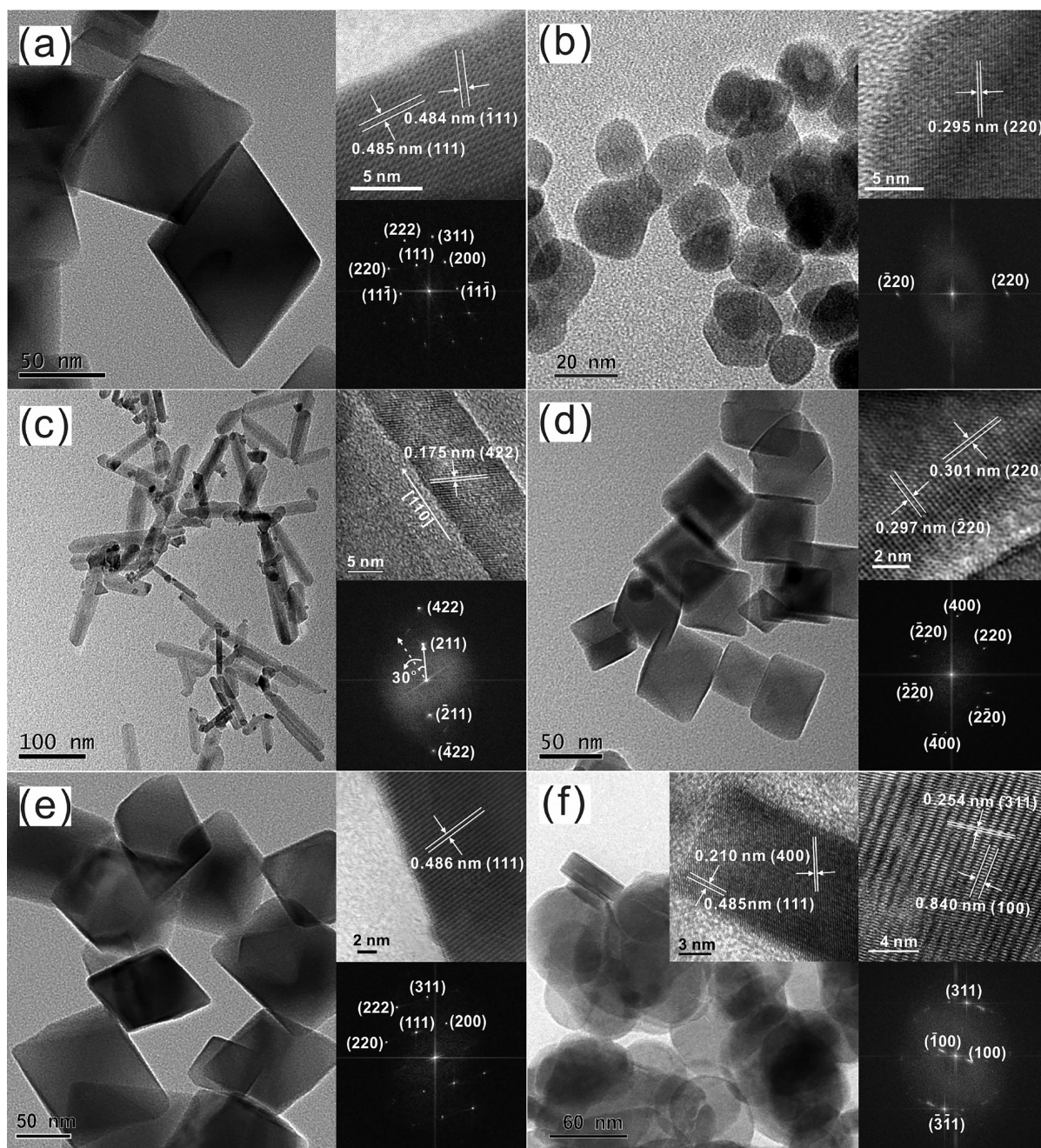


Figure 3. TEM, HRTEM images (upper right insets), and Fourier transforms images (lower right insets) of the magnetite NPs, (a): Fe₃O₄-N, (b): Fe₃O₄-S, (c): Fe₃O₄-R, (d): Fe₃O₄-C, (e): Fe₃O₄-O, (f): Fe₃O₄-P.

To further investigate the interaction between the atomic nucleus and the surrounding environment of the magnetite structure, the Mössbauer spectra of representative samples Fe₃O₄-N, Fe₃O₄-O, Fe₃O₄-R, and Fe₃O₄-P were dissected. The optimum fitted spectra are shown in Figure 5, and the assignments, sites A and B, denote the tetrahedral site and octahedral site of a typical magnetite crystal structure, respectively. The fitted hyperfine parameters of subspectra, such as isomer shifts (IS), quadruple splittings (QS), hyperfine magnetic fields (H_{hf}), and resonance half-height line widths (W) are given in Table S3. The Mössbauer spectra of Fe₃O₄-N (Figure 5a) and Fe₃O₄-O (Figure 5b) were fitted with two hyperfine magnetic sextets (line-area ratios 3:2:1:1:2:3) as well as a quadrupole doublet. Typically, these two sextets represent

$^{\text{tet}}\text{Fe}^{3+}$ and $^{\text{oct}}\text{Fe}^{2.5+}$ (i.e., Fe²⁺ and Fe³⁺ with delocalized d-electrons) in an inverse spinel structure.⁴⁶ Accordingly, the H_{hf} and IS were around 490 kOe and 0.29 mm s⁻¹ for $^{\text{tet}}\text{Fe}^{3+}$ and about 456 kOe and 0.65 mm s⁻¹ for $^{\text{oct}}\text{Fe}^{2.5+}$ (Table S3). These values match very well with the reported values for well-crystallized Fe₃O₄,^{47,48} suggesting that the Fe₃O₄-N and Fe₃O₄-R were not γ -Fe₂O₃, but Fe₃O₄. Furthermore, the symmetric quadrupole doublet in Figure 5a,b may be assigned to well-dispersed ultrafine particles of Fe₃O₄ experiencing superparamagnetic relaxation. In contrast, the Mössbauer spectra of Fe₃O₄-R and Fe₃O₄-P were fitted to several minor sextets (sextet 3–6) and two quadrupole doublets. These differences were mainly due to the changes in sizes, morphologies, and structural disorder of the Fe₃O₄ samples,

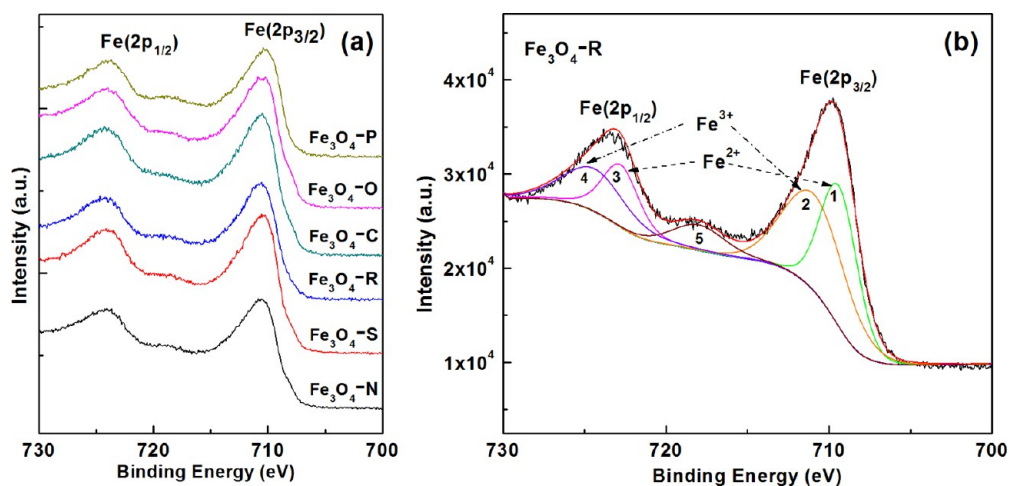


Figure 4. (a): XPS spectra (Fe 2p) of the Fe_3O_4 NPs, (b): an example (Fe_3O_4 -R) of a Fe 2p spectrum fitting result in the assignment of Fe^{2+} and Fe^{3+} .

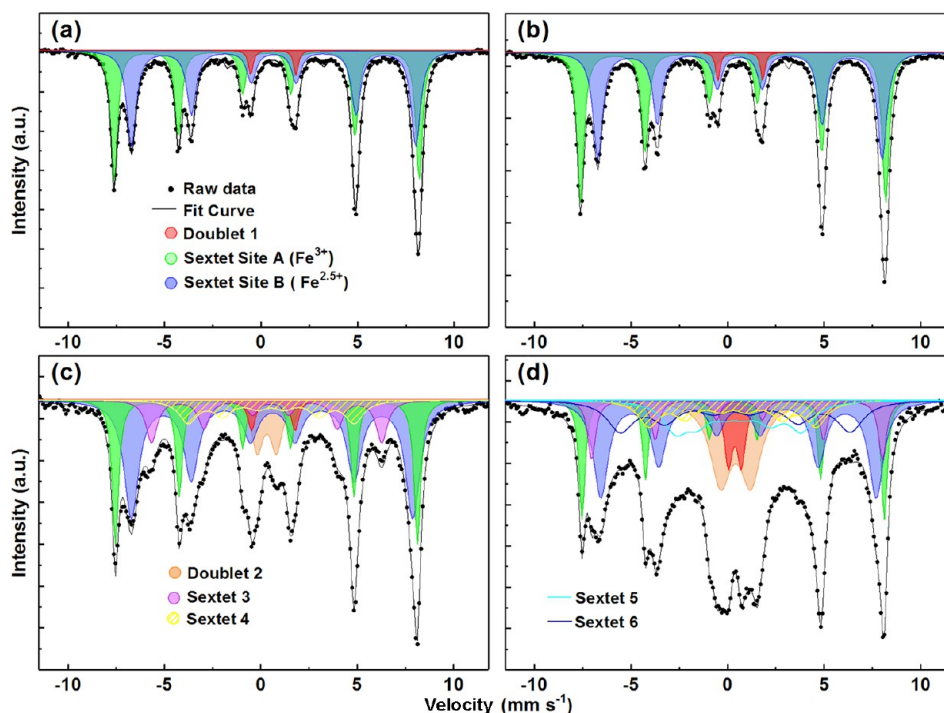


Figure 5. Room-temperature (297 K) ^{57}Fe Mössbauer spectra of magnetite NPs, in which the spectra were fitted with several sextets and doublets. (a): Fe_3O_4 -N, (b): Fe_3O_4 -O, (c): Fe_3O_4 -R, and (d): Fe_3O_4 -P.

leading to the significant impact on the atomic local environment of iron. Apart from the two main sextets, the subspectra were also fitted with several less intense hyperfine fields ($H_f \leq 442.10$ kOe, Table S3), which might be due to the following three reasons. First, the presence of a small amount of $\gamma\text{-Fe}_2\text{O}_3$ on the surface of the Fe_3O_4 NPs was supported by the XPS analysis as mentioned above. Second, the nanosize effect derived from a fraction of the smaller particles of Fe_3O_4 . Third, the spin state of iron ions varied with the preponderant growth orientation of the microstructure, resulting in multifractal sextets. Wider quadruple splittings can be seen in Figure 5c,d, indicating the electric field environment around these particular atoms is asymmetrical compared with that of octahedron Fe_3O_4 . Specifically, the rod-like and nanoplate Fe_3O_4 possessed higher surface energy, enhanced quantum effects, and stronger

relaxation effects in comparison with octahedral Fe_3O_4 . Note that, according to the chemical formula $[\text{Fe}^{3+}]_{\text{tet}}[\text{Fe}^{2+}\text{Fe}^{3+}]_{\text{oct}}\text{O}_4$, the relative intensity ($R = I_A/I_B$) of the first and the second sextets in the Mössbauer spectrum should be close to 1:2. However, the R value of these lines was greater than 0.5 (Table S3). One reason for this could be the nonstoichiometry of magnetite, which is actually described by the formula $\text{Fe}_{3-\delta}\text{O}_4$, where δ is the fraction of vacancies.⁴⁹ This phenomenon also has been observed in Mössbauer spectra of Fe_3O_4 by many researchers.^{49–51}

Magnetic measurements of Fe_3O_4 NPs were conducted by measuring the applied field dependence of magnetization (Figure 6). The magnetic hysteresis loops (M - H curves) at 300 K illustrate that Fe_3O_4 NPs had strong magnetic responses to a varying magnetic field. The magnified view of the M - H

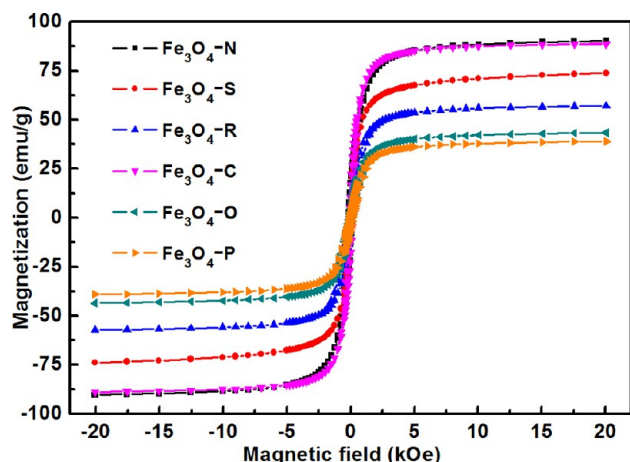
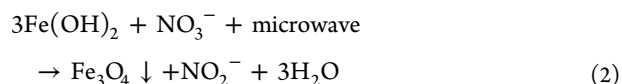
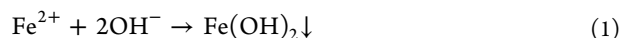


Figure 6. Room-temperature (300 K) magnetic hysteresis loops of the Fe_3O_4 NPs.

curves, with characteristic reversible hysteresis loops and ferromagnetic behavior, is shown in Figure S4. The saturation magnetization (M_s) and coercivity (H_c) values were 90.2 emu g^{-1} and 180 Oe , respectively, for $\text{Fe}_3\text{O}_4\text{-N}$ synthesized by coprecipitation (Table S4). The magnetization value is in good agreement with the theoretical value of bulk magnetite ($\sim 90 \text{ emu g}^{-1}$).⁵² As for the samples synthesized by the microwave-assisted oxidation process, both values of M_s and H_c were distinctly different from each other. The magnetization of $\text{Fe}_3\text{O}_4\text{-O}$ (43.4 emu g^{-1}) and $\text{Fe}_3\text{O}_4\text{-P}$ (39.0 emu g^{-1}) were much lower than $\text{Fe}_3\text{O}_4\text{-N}$, while the magnetization of $\text{Fe}_3\text{O}_4\text{-C}$ (88.7 emu g^{-1}) was the highest of the samples. These results imply that the magnetic properties were shape dependent and sensitive to particle size. This fact is likely caused by both the magnetic anisotropy and the magnetic interparticle interaction strength between NPs. Specifically, the reduced M_s may be due to (i) the high anisotropy of the Fe_3O_4 nanostructure, which prevents it from magnetizing in directions other than along the easy magnetic axes, i.e. [111] and [110] directions,⁴⁷ and (ii) the decrease in particle size would lead to more surface spin disorder and, consequently, a reduction in the M_s .⁵³

Based on our results, morphology-controlled magnetite NPs were successfully synthesized, suggesting the microwave

irradiation oxidation process effectively provided means to tailor the shapes of Fe_3O_4 NPs. In addition to the lower crystallization temperature ($95 \text{ }^\circ\text{C}$), the acceleration of the crystallization process by hot spots and superheating effects was very noticeable. During the nucleation and growth differentiation process, the PEG-600 and PVP acted as a soft template and played a vital role in determining the final shape of the resultant nanostructure. The main reaction mechanisms may include the following:



3.2. UVA/Fenton Catalytic Activity of Fe_3O_4 NPs toward a Probe Molecule.

The oxidative degradation of AOII was used as a probe reaction to investigate the UVA/Fenton catalytic performances of the Fe_3O_4 samples (Figure 7). Before adding H_2O_2 and UVA irradiation, the removal rate through adsorption was about $0.9\% \sim 5.4\%$ by the Fe_3O_4 samples. In the absence of a Fe_3O_4 catalyst and H_2O_2 (blank), the concentration of AOII did not obviously decrease. Approximately 20% of AOII was reduced after 180 min UVA irradiation in H_2O_2 . After the introduction of Fe_3O_4 NPs to the UVA/ H_2O_2 system, the decolorization of AOII was significantly enhanced, and the degradation process was described as a pseudo-first order rate mechanism (Figure S5). Fe_3O_4 samples prepared by microwave irradiation oxidation showed distinctly stronger UVA/Fenton catalytic activity than the coprecipitation sample. The AOII removal efficiencies obeyed the following order under our test conditions: $\text{Fe}_3\text{O}_4\text{-S} > \text{Fe}_3\text{O}_4\text{-P} > \text{Fe}_3\text{O}_4\text{-O} \approx \text{Fe}_3\text{O}_4\text{-C} > \text{Fe}_3\text{O}_4\text{-R} > \text{Fe}_3\text{O}_4\text{-N}$. Compared to the reaction rate of $\text{Fe}_3\text{O}_4\text{-N}$ ($t_{1/2} = 86.5 \text{ min}$, Table S5), only 8–10 min were needed to remove 50% of AOII in $\text{Fe}_3\text{O}_4\text{-S}$ and $\text{Fe}_3\text{O}_4\text{-P}$ reaction systems. This reaction rate was 8–10 times faster than that of $\text{Fe}_3\text{O}_4\text{-N}$. Even for $\text{Fe}_3\text{O}_4\text{-R}$, the $t_{1/2}$ for AOII removal was half the reaction rate of $\text{Fe}_3\text{O}_4\text{-N}$. It is worth noting that the variation in catalytic efficiency was negatively correlated with the average grain size (Table 1), suggesting that the nanoparticle size is an important factor for the efficiency of these Fe_3O_4 NPs. The highest decolorization

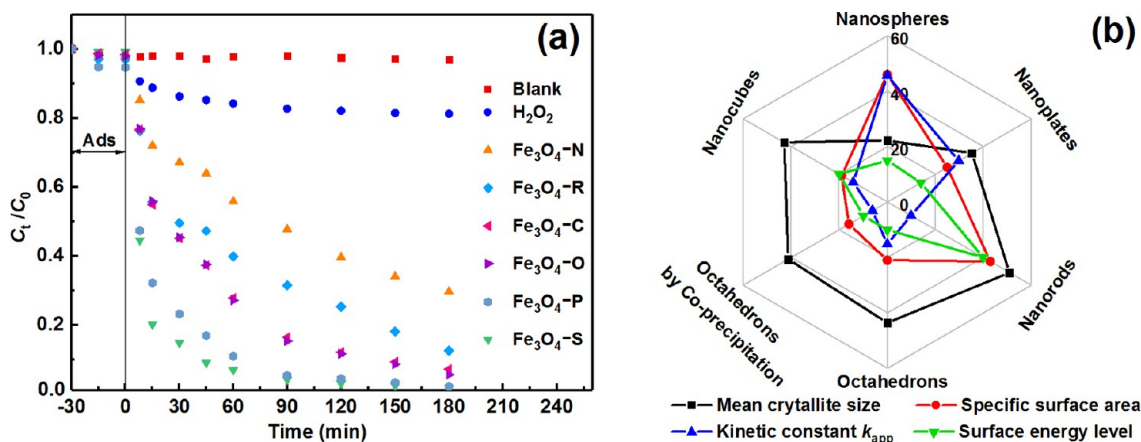
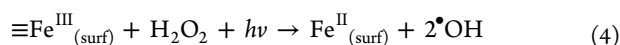
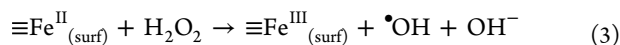


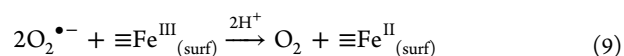
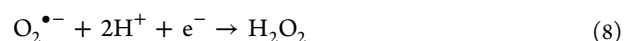
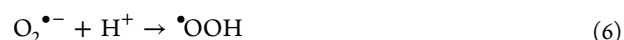
Figure 7. (a): Decolorization of AOII through UVA/Fenton reaction catalyzed by Fe_3O_4 NPs with different morphology (AOII: 100 mg L^{-1} , H_2O_2 : 20 mmol L^{-1} , catalyst: 0.5 g L^{-1} , pH: 3.0, $25 \text{ }^\circ\text{C}$); (b) Relationships between the morphology, mean crystallite size, BET-specific surface area, energy level of exposed facets and catalytic activity (k_{app}) of Fe_3O_4 NPs (the energy level of exposed facets is digitized according to the sequence of surface energy, i.e., $\gamma\{111\} < \gamma\{100\} < \gamma\{110\} < \gamma\{220\} < \gamma\{112\}$).

rate of AOII by UVA/Fenton process was obtained for Fe₃O₄-S, which has the smallest particle size/crystallite size and the highest BET specific surface area. Fe₃O₄-C and Fe₃O₄-O systems, which have similar BET specific surface areas, displayed almost equally matched catalytic efficiency. However, according to the surface atomic configuration in a unit cell of Fe₃O₄, the {100} and {111} planes contained only Fe²⁺ cations, and the exposed {111} facets on octahedrons had more Fe²⁺ than the {100} facets on cubic particles.⁵⁴ Therefore, similar catalytic efficiency was observed even though the average particle size of Fe₃O₄-O was more than twice the particle size of Fe₃O₄-C. The BET-specific surface area of rod-like NPs was higher than that of nanoplate NPs; however, the rod-like NPs showed weaker catalytic activity than the nanoplates. This may be because different morphologies of NPs have different fractions of reactive Fe ions located at the predominantly exposed planes. From the previous analysis of HRTEM (Figure 3), the dominant exposed planes of Fe₃O₄-R NPs were {112} and {110}, while {111} and {100} were the dominant exposed planes in the Fe₃O₄-P NPs. Because {110} and {112} planes are composed mainly of Fe³⁺ rather than Fe²⁺, the dominant presence of {111} planes in the Fe₃O₄-P NPs, which are rich in catalytically active Fe²⁺, would lead to stronger catalytic activity. Generally, the difference in removal rates suggests the UVA/Fenton catalytic activity of Fe₃O₄ was dependent on grain size, specific surface area, micromorphology, and exposed crystal planes. Smaller crystallite size, larger surface area and the exposed facets with relatively lower surface energy were conducive to enhancing the UVA/Fenton catalytic activity of Fe₃O₄ NPs and vice versa (Figure 7b). The improved catalytic activity originated from the intrinsically greater reactivity of {111} and {100} dominate surfaces compared to that of {110} and {112} dominate surfaces because of the Fenton-like reaction of ≡Fe^{II}_(surf) and H₂O₂ on the nanocrystal surface. As we know, the ≡Fe^{II}_(surf) located at nanocrystals' surface is likely to be chemically very active. Therefore, a possible explanation was proposed: (i) the H₂O₂ is easily attracted by Fe₃O₄ NPs' surface, promoting ≡Fe^{II}_(surf) to join the UVA/Fenton catalytic degradation process (eq 3), which results in the enhancement of catalytic activity of Fe₃O₄-S and Fe₃O₄-P with exposed {111} and {100} facets. (ii) under UVA irradiation, electron/hole pairs can be photogenerated on the Fe₃O₄ surface. Then photogenerated electrons can be trapped by H₂O₂ and the generated ≡Fe^{III}_(surf) forming ≡Fe^{II}_(surf) and •OH (eq 4), which further accelerated the degradation process. We should mention that, in all cases, the Fe leaching after reaction was less than 2.63 mg L⁻¹ (Table S6), and <0.72 wt % compared to the Fe content in the added Fe₃O₄ NPs, indicating that the contribution of the dissolved Fe ions to the degradation process was negligible.



The time-resolved UV-vis absorption spectroscopy (Figure S6) shows that AOII was progressively reduced, and the two main peaks at approximately 484 and 310 nm diminished simultaneously, indicating gradual destruction of the azo and naphthalene structure of AOII. It has been demonstrated that the hydroxyl-radical-mediated mechanism played a crucial role in the heterogeneous photo-Fenton reaction systems (eq 3 and 4).⁵⁵ Herein, the dynamic assessment of •OH and O₂^{•-} by ESR

showed no signal in dark conditions for all samples, but clear ESR four-line patterns assigned to DMPO-•OH⁵⁶ (Figure S7) and DMPO-O₂^{•-} adducts⁵⁷ (Figure S8) gradually evolved under UV light irradiation. Note that almost no DMPO-O₂^{•-} signals were observed, and a slight DMPO-•OH signal was detected in the UVA/H₂O₂ system. However, the signal intensity remarkably enhanced in the presence of Fe₃O₄ NPs, which demonstrated that •OH and O₂^{•-} oxidative radicals coexist and participate in the AOII degradation process. The yield of •OH and O₂^{•-} radicals catalyzed by Fe₃O₄ NPs increased significantly as the reaction continued, and the catalytic activity was in the following sequence: Fe₃O₄-S > Fe₃O₄-P > Fe₃O₄-O ≈ Fe₃O₄-C > Fe₃O₄-R > Fe₃O₄-N. This sequence is in good agreement with removal performance. These findings imply that the improved generation of •OH and O₂^{•-} radicals resulted in higher removal efficiency of AOII in the heterogeneous UVA/Fenton system. By adding the •OH scavenger dimethyl sulfoxide to the reaction system containing Fe₃O₄-S (Figure S9), the removal efficiency of AOII declined sharply by more than 85%. This fully proved that the AOII degradation mainly depended on the generated •OH radicals, and the residual removal efficiency of 15% might be due to O₂^{•-} or other reactive species. This also explains why the exposed facets with more Fe ions possessed stronger catalytic performance. It has been widely reported^{58,59} that photo-generated electrons (e⁻) are usually scavenged by O₂ to yield superoxide radical O₂^{•-}/•OOH (eqs 5 and 6). Moreover, O₂^{•-} may contribute to the H₂O₂ regeneration (eq 7 and 8) and ≡Fe^{III}_(surf) reduction (eq 9) during photocatalytic reactions. Consequently, O₂^{•-} can be detected in the reaction system and should not be ignored.



The Fe₃O₄ NPs were easily separated and collected after treatment, efficiently preventing the undesirable release of NPs into the environment. More importantly, these Fe₃O₄ NPs maintained good stability and reusability. Take Fe₃O₄-S for example, there still more than 90% AOII was removed by the recovered catalyst after four recycles (Figure S10), with only a slight decrease of the catalytic activity. Additionally, XRD (Figure S11) and SEM (Figure S12) analyses also confirmed the chemical composition and morphological stability of Fe₃O₄-S NPs during the recycles.

4. CONCLUSIONS

Morphology-controlled magnetite NPs (i.e., nanospheres, nanorods, nanocubes, nano-octahedrons, and nanoplates) have been successfully synthesized by the microwave-assisted oxidation process. HRTEM analysis and Mössbauer spectra indicated that the predominantly exposed crystal facets and the local environment of iron atoms were sufficiently influenced by the morphology and grain size. The evaluation of the heterogeneous UVA/Fenton degradation process showed that Fe₃O₄ NPs prepared by microwave irradiation oxidation had distinctly stronger catalytic activities than that of Fe₃O₄ NPs

prepared by coprecipitation, and the catalytic activity obeyed the following order: nanospheres > nanoplates > nano-octahedrons \approx nanocubes > nanorods > nano-octahedrons (by coprecipitation). Smaller particle size, larger surface area, and more exposure of reactive facets {111} were conducive to enhanced UVA/Fenton catalytic activity of Fe₃O₄ NPs. The ESR results demonstrated the participation of \bullet OH and O₂^{•-} radicals in AOII degradation process, and the former played a dominant role and constrained the degradation efficiency. In addition, the Fe₃O₄ nanoparticles presented satisfying stability and reusability in a heterogeneous UVA/Fenton reaction, with limited loss in catalytic activity. These shape-controlled nanomagnetites are promising heterogeneous UV/Fenton catalysts for effectively treating nonbiodegradable organic pollutants.

■ ASSOCIATED CONTENT

Supporting Information

The Supporting Information is available free of charge on the ACS Publications website at DOI: 10.1021/acsami.7b06925.

Additional characterizations (including HRTEM analysis of the Fe₃O₄-R, fitting results of Fe 2p and O 1s spectra, M-H curve, the fitted kinetics process, UV-vis spectra, and ESR spectra) and referenced supplementary tables (PDF)

■ AUTHOR INFORMATION

Corresponding Author

*E-mail for L.Yu: gych@gdut.edu.cn. Tel: +86 20 39322202. Fax: +86 20 39322231.

ORCID

Lin Yu: 0000-0001-6187-6514

Notes

The authors declare no competing financial interest.

■ ACKNOWLEDGMENTS

We gratefully acknowledge the financial support from the Natural Science Foundation of China (No. 41602031) and the China Postdoctoral Science Foundation Funded Project (No. 2016M592464).

■ REFERENCES

- (1) Baeza, A.; Guillena, G.; Ramón, D. J. Magnetite and Metal-impregnated Magnetite Catalysts in Organic synthesis: A Very Old Concept with New Promising Perspectives. *ChemCatChem* **2016**, *8*, 49–67.
- (2) Wu, W.; Wu, Z.; Yu, T.; Jiang, C.; Kim, W.-S. Recent progress on magnetic iron oxide nanoparticles: synthesis, surface functional strategies and biomedical applications. *Sci. Technol. Adv. Mater.* **2015**, *16*, 023501.
- (3) Hou, L.; Zhang, Q.; Jérôme, F.; Duprez, D.; Zhang, H.; Royer, S. Shape-controlled Nanostructured Magnetite-type Materials as Highly Efficient Fenton Catalysts. *Appl. Catal., B* **2014**, *144*, 739–749.
- (4) Li, Y.; Shen, W. Morphology-dependent Nanocatalysts: Rod-shaped Oxides. *Chem. Soc. Rev.* **2014**, *43*, 1543–1574.
- (5) Hu, L.; Sun, K.; Peng, Q.; Xu, B.; Li, Y. Surface Active Sites on Co₃O₄ Nanobelt and Nanocube Model Catalysts for CO Oxidation. *Nano Res.* **2010**, *3*, 363–368.
- (6) Gao, Q.-X.; Wang, X.-F.; Di, J.-L.; Wu, X.-C.; Tao, Y.-R. Enhanced Catalytic Activity of α -Fe₂O₃ Nanorods Enclosed with {110} and {001} Planes for Methane Combustion and CO Oxidation. *Catal. Sci. Technol.* **2011**, *1*, 574–577.
- (7) Ji, W.; Li, M.; Zhang, G.; Wang, P. Correction: Controlled Synthesis of Bi₂₅FeO₄₀ with Different Morphologies: Growth Mechanism and Enhanced Photo-Fenton Catalytic Properties. *Dalton T.* **2017**, *46*, 3770–3770.
- (8) Zhong, Y.; Liang, X.; Tan, W.; Zhong, Y.; He, H.; Zhu, J.; Yuan, P.; Jiang, Z. A comparative Study About the Effects of Isomorphous Substitution of Transition Metals (Ti, Cr, Mn, Co and Ni) on the UV/Fenton Catalytic Activity of magnetite. *J. Mol. Catal. A: Chem.* **2013**, *372*, 29–34.
- (9) Munoz, M.; de Pedro, Z. M.; Casas, J. A.; Rodriguez, J. J. Preparation of Magnetite-based Catalysts and Their Application in Heterogeneous Fenton Oxidation -A review. *Appl. Catal., B* **2015**, *176–177*, 249–265.
- (10) Nguyen, X. S.; Zhang, G.; Yang, X. Mesocrystalline Zn-Doped Fe₃O₄ Hollow Submicrospheres: Formation Mechanism and Enhanced Photo-Fenton Catalytic Performance. *ACS Appl. Mater. Interfaces* **2017**, *9*, 8900–8909.
- (11) Yuan, P.; Fan, M.; Yang, D.; He, H.; Liu, D.; Yuan, A.; Zhu, J.; Chen, T. Montmorillonite-supported Magnetite Nanoparticles for the Removal of Hexavalent Chromium [Cr (VI)] from Aqueous Solutions. *J. Hazard. Mater.* **2009**, *166*, 821–829.
- (12) Costa, R. C.; Lelis, M. d. F. F.; Oliveira, L. C.; Fabris, J. D.; Ardisson, J. D.; Rios, R. R.; Silva, C. N.; Lago, R. M. Remarkable Effect of Co and Mn on the Activity of Fe_{3-x}M_xO₄ Promoted Oxidation of Organic Contaminants in Aqueous Medium with H₂O₂. *Catal. Commun.* **2003**, *4*, 525–529.
- (13) Liang, X.; Zhong, Y.; Zhu, S.; Zhu, J.; Yuan, P.; He, H.; Zhang, J. The Decolorization of Acid Orange II in Non-homogeneous Fenton Reaction Catalyzed by Natural Vanadium–titanium Magnetite. *J. Hazard. Mater.* **2010**, *181*, 112–120.
- (14) Zhong, Y.; Liang, X.; Zhong, Y.; Zhu, J.; Zhu, S.; Yuan, P.; He, H.; Zhang, J. Heterogeneous UV/Fenton Degradation of TBBPA Catalyzed by Titanomagnetite: Catalyst Characterization, Performance and Degradation products. *Water Res.* **2012**, *46*, 4633–4644.
- (15) Su, D. W.; Ahn, H. J.; Wang, G. X. One-dimensional Magnetite Fe₃O₄ Nanowires as Electrode Material for Li-ion Batteries with Improved Electrochemical Performance. *J. Power Sources* **2013**, *244*, 742–746.
- (16) Lu, A. H.; Salabas, E. L.; Schuth, F. Magnetic Nanoparticles: Synthesis, Protection, Functionalization, and Application. *Angew. Chem., Int. Ed.* **2007**, *46*, 1222–44.
- (17) Daou, T.; Pourroy, G.; Begin-Colin, S.; Greneche, J.; Ulhaq-Bouillet, C.; Legaré, P.; Bernhardt, P.; Leuvrey, C.; Rogez, G. Hydrothermal Synthesis of Monodisperse Magnetite Nanoparticles. *Chem. Mater.* **2006**, *18*, 4399–4404.
- (18) Chin, A. B.; Yaacob, I. I. Synthesis and Characterization of Magnetic Iron Oxide Nanoparticles via w/o Microemulsion and Massart's Procedure. *J. Mater. Process. Technol.* **2007**, *191*, 235–237.
- (19) Francois, N. J.; Allo, S.; Jacobo, S. E.; Daraio, M. E. Composites of Polymeric Gels and Magnetic Nanoparticles: Preparation and Drug Release Behavior. *J. Appl. Polym. Sci.* **2007**, *105*, 647–655.
- (20) Maity, D.; Kale, S.; Kaul-Ghanekar, R.; Xue, J.-M.; Ding, J. Studies of Magnetite Nanoparticles Synthesized by Thermal Decomposition of Iron (III) Acetylacetonate in Tri (ethylene glycol). *J. Magn. Magn. Mater.* **2009**, *321*, 3093–3098.
- (21) Wang, N.; Zhu, L.; Wang, D.; Wang, M.; Lin, Z.; Tang, H. Sono-assisted Preparation of Highly-efficient Peroxidase-like Fe₃O₄ Magnetic Nanoparticles for Catalytic Removal of Organic Pollutants with H₂O₂. *Ultrason. Sonochem.* **2010**, *17*, 526–533.
- (22) Yang, C.; Wu, J.; Hou, Y. Fe₃O₄ Nanostructures: Synthesis, Growth Mechanism, Properties and Applications. *Chem. Commun. (Cambridge, U. K.)* **2011**, *47*, 5130–41.
- (23) Sun, S. H.; Zeng, H. Size-controlled Synthesis of Magnetite Nanoparticles. *J. Am. Chem. Soc.* **2002**, *124*, 8204–8205.
- (24) Zhang, L.; Wu, J.; Liao, H.; Hou, Y.; Gao, S. Octahedral Fe₃O₄ Nanoparticles and Their Assembled Structures. *Chem. Commun.* **2009**, *29*, 4378–4380.

- (25) Yang, H.; Ogawa, T.; Hasegawa, D.; Takahashi, M. Synthesis and Magnetic Properties of Monodisperse Magnetite Nanocubes. *J. Appl. Phys.* **2008**, *103*, 07D526–07D526–3.
- (26) Xu, Z.; Shen, C.; Hou, Y.; Gao, H.; Sun, S. Oleylamine as Both Reducing Agent and Stabilizer in a Facile Synthesis of Magnetite Nanoparticles. *Chem. Mater.* **2009**, *21*, 1778–1780.
- (27) Dresco, P. A.; Zaitsev, V. S.; Gambino, R. J.; Chu, B. Preparation and Properties of Magnetite and Polymer Magnetite Nanoparticles. *Langmuir* **1999**, *15*, 1945–1951.
- (28) Dallinger, D.; Kappe, C. O. Microwave-assisted Synthesis in Water as Solvent. *Chem. Rev.* **2007**, *107*, 2563–2591.
- (29) Chung, C.-C.; Chung, T.-W.; Yang, T. C.-K. Rapid Synthesis of Titania Nanowires by Microwave-assisted Hydrothermal Treatments. *Ind. Eng. Chem. Res.* **2008**, *47*, 2301–2307.
- (30) Hu, X.; Yu, J. C.; Gong, J.; Li, Q.; Li, G. α -Fe₂O₃ Nanorings Prepared by a Microwave-assisted Hydrothermal Process and Their Sensing Properties. *Adv. Mater.* **2007**, *19*, 2324–2329.
- (31) Xu, L.; Ding, Y.-S.; Chen, C.-H.; Zhao, L.; Rimkus, C.; Joesten, R.; Suib, S. L. 3D Flowerlike α -nickel Hydroxide with Enhanced Electrochemical Activity Synthesized by Microwave-assisted Hydrothermal Method. *Chem. Mater.* **2008**, *20*, 308–316.
- (32) Pan, J.; Li, M.; Luo, Y.; Wu, H.; Zhong, L.; Wang, Q.; Li, G. Microwave-assisted Hydrothermal Synthesis of V₂O₅ Nanorods Assemblies with an Improved Li-ion Batteries Performance. *Mater. Res. Bull.* **2016**, *74*, 90–95.
- (33) Ai, Z.; Deng, K.; Wan, Q.; Zhang, L.; Lee, S. Facile Microwave-assisted Synthesis and Magnetic and Gas Sensing Properties of Fe₃O₄ Nanoroses. *J. Phys. Chem. C* **2010**, *114*, 6237–6242.
- (34) Wang, Z. Transmission Electron Microscopy of Shape-controlled Nanocrystals and Their Assemblies. *J. Phys. Chem. B* **2000**, *104*, 1153–1175.
- (35) Xiong, Y.; Xia, Y. Shape-controlled synthesis of metal nanostructures: the case of palladium. *Adv. Mater.* **2007**, *19*, 3385–3391.
- (36) Mahmoud, M. A.; El-Sayed, M. A.; Gao, J.; Landman, U. High-frequency Mechanical Stirring Initiates Anisotropic Growth of Seeds Requisite for Synthesis of Asymmetric Metallic Nanoparticles like Silver Nanorods. *Nano Lett.* **2013**, *13*, 4739–4745.
- (37) Feng, J.; Zeng, H. C. Size-controlled growth of Co₃O₄ nanocubes. *Chem. Mater.* **2003**, *15*, 2829–2835.
- (38) Ho, C.-H.; Tsai, C.-P.; Chung, C.-C.; Tsai, C.-Y.; Chen, F.-R.; Lin, H.-J.; Lai, C.-H. Shape-Controlled Growth and Shape-Dependent Cation Site Occupancy of Monodisperse Fe₃O₄ Nanoparticles. *Chem. Mater.* **2011**, *23*, 1753–1760.
- (39) Khurshid, H.; Li, W.; Chandra, S.; Phan, M. H.; Hadjipanayis, G. C.; Mukherjee, P.; Srikanth, H. Mechanism and Controlled Growth of Shape and Size Variant Core/shell FeO/Fe₃O₄ Nanoparticles. *Nanoscale* **2013**, *5*, 7942–52.
- (40) Xiong, Y.; McLellan, J. M.; Chen, J.; Yin, Y.; Li, Z.-Y.; Xia, Y. Kinetically Controlled Synthesis of Triangular and Hexagonal Nanoplates of Palladium and Their SPR/SERS Properties. *J. Am. Chem. Soc.* **2005**, *127*, 17118–17127.
- (41) Chen, Y.-J.; Xiao, G.; Wang, T.-S.; Ouyang, Q.-Y.; Qi, L.-H.; Ma, Y.; Gao, P.; Zhu, C.-L.; Cao, M.-S.; Jin, H.-B. Porous Fe₃O₄/Carbon Core/Shell Nanorods: Synthesis and Electromagnetic Properties. *J. Phys. Chem. C* **2011**, *115*, 13603–13608.
- (42) Tiwari, S.; Prakash, R.; Choudhary, R.; Phase, D. Oriented Growth of Fe₃O₄ Thin Film on Crystalline and Amorphous Substrates by Pulsed laser Deposition. *J. Phys. D: Appl. Phys.* **2007**, *40*, 4943.
- (43) Scott, T.; Allen, G.; Heard, P.; Randell, M. Reduction of U (VI) to U (IV) on the Surface of Magnetite. *Geochim. Cosmochim. Acta* **2005**, *69*, 5639–5646.
- (44) Guo, S.; Yuan, N.; Zhang, G.; Yu, J. C. Graphene Modified Iron Sludge Derived from Homogeneous Fenton Process as An Efficient Heterogeneous Fenton Catalyst for Degradation of Organic Pollutants. *Microporous Mesoporous Mater.* **2017**, *238*, 62–68.
- (45) Chandra, V.; Park, J.; Chun, Y.; Lee, J. W.; Hwang, I. C.; Kim, K. S. Water-dispersible Magnetite-reduced Graphene Oxide Composites for Arsenic Removal. *ACS Nano* **2010**, *4*, 3979–3986.
- (46) Zhou, H. W.; Yin, J.; Nie, Z. H.; Yang, Z. J.; Li, D. J.; Wang, J. H.; Liu, X.; Jin, C. Z.; Zhang, X. X.; Ma, T. L. Earth-abundant and Nano-micro Composite Catalysts of Fe₃O₄@reduced Graphene Oxide for Green and Economical Mesoscopic Photovoltaic Devices with High Efficiencies up to 9%. *J. Mater. Chem. A* **2016**, *4*, 67–73.
- (47) Wang, J.; Chen, Q.; Zeng, C.; Hou, B. Magnetic-field-induced Growth of Single-Crystalline Fe₃O₄ Nanowires. *Adv. Mater.* **2004**, *16*, 137–140.
- (48) Gorski, C. A.; Scherer, M. M. Determination of Nanoparticulate Magnetite Stoichiometry by Mössbauer Spectroscopy, Acidic Dissolution, and Powder X-ray Diffraction: A critical Review. *Am. Mineral.* **2010**, *95*, 1017–1026.
- (49) da Costa, G. M.; De Grave, E.; De Bakker, P. M. A.; Vandenberghe, R. E. Influence of Nonstoichiometry and the Presence of Maghemite on the Mössbauer Spectrum of Magnetite†. *Clays Clay Miner.* **1995**, *43*, 656–668.
- (50) Daniels, J. M.; Rosencwaig, A. Mössbauer Spectroscopy of Stoichiometric and Non-stoichiometric Magnetite. *J. Phys. Chem. Solids* **1969**, *30*, 1561–1571.
- (51) Johnson, C. E.; Johnson, J. A.; Hah, H. Y.; Cole, M.; Gray, S.; Kolesnichenko, V.; Kucheryavy, P.; Goloverda, G. Mössbauer Studies of Stoichiometry of Fe₃O₄: Characterization of Nanoparticles for Biomedical Applications. *Hyperfine Interact.* **2016**, *237*, 27.
- (52) Chikazumi, S. *Physics of Magnetism*; Wiley: New York, 1964; p 100.
- (53) Rajendran, M.; Pullar, R. C.; Bhattacharya, A. K.; Das, D.; Chintalapudi, S. N.; Majumdar, C. K. Magnetic Properties of Nanocrystalline CoFe₂O₄ Powders Prepared at Room Temperature: Variation with Crystallite Size. *J. Magn. Magn. Mater.* **2001**, *232*, 71–83.
- (54) Xie, X.; Shen, W. Morphology Control of Cobalt Oxide Nanocrystals for Promoting Their Catalytic Performance. *Nanoscale* **2009**, *1*, 50–60.
- (55) Zhong, Y. H.; Liang, X. L.; Zhong, Y.; Zhu, J. X.; Zhu, S. Y.; Yuan, P.; He, H. P.; Zhang, J. Heterogeneous UV/Fenton Degradation of TBBPA Catalyzed by Titanomagnetite: Catalyst Characterization, Performance and Degradation Products. *Water Res.* **2012**, *46*, 4633–44.
- (56) Wang, H.; Su, Y.; Zhao, H.; Yu, H.; Chen, S.; Zhang, Y.; Quan, X. Photocatalytic Oxidation of Aqueous Ammonia Using Atomic Single Layer Graphitic-C₃N₄. *Environ. Sci. Technol.* **2014**, *48*, 11984–11990.
- (57) Su, F.; Mathew, S. C.; Lipner, G.; Fu, X.; Antonietti, M.; Blechert, S.; Wang, X. mpg-C₃N₄-Catalyzed Selective Oxidation of Alcohols Using O₂ and Visible Light. *J. Am. Chem. Soc.* **2010**, *132*, 16299–16301.
- (58) Hu, X.; Ji, H.; Chang, F.; Luo, Y. Simultaneous Photocatalytic Cr(VI) Reduction and 2,4,6-TCP Oxidation over g-C₃N₄ under Visible Light Irradiation. *Catal. Today* **2014**, *224*, 34–40.
- (59) Wang, X.; Tian, H.; Yang, Y.; Wang, H.; Wang, S.; Zheng, W.; Liu, Y. Reduced Graphene Oxide/CdS for Efficiently Photocatalytic Degradation of Methylene blue. *J. Alloys Compd.* **2012**, *524*, 5–12.